



AIAA 98-0306

**Developments in Picosecond Pump/Probe
Diagnostics**

M. Linne and T. Settersten
Center for Combustion and Environmental Research
Colorado School of Mines
Golden, Colorado

J. Gord, Wright Laboratory,
Aero Power and Propulsion Directorate,
Wright Patterson AFB, Ohio

G. Fiechtner,
Innovative Scientific Solutions, Inc.
Dayton, Ohio

**36th Aerospace Sciences
Meeting & Exhibit**
January 12–15, 1998 / Reno, NV

DEVELOPMENTS IN PICOSECOND PUMP/PROBE DIAGNOSTICS

M. Linne and T. Settersten
Center for Combustion and Environmental Research
Colorado School of Mines, Golden, CO

J. Gord
Wright Laboratories, Wright Patterson AFB, OH

G. Fiechtner
Innovative Scientific Solutions Inc., Dayton, OH

Abstract

This paper describes further developments in picosecond pump/probe combustion diagnostics. The rate equation formalism originally used to model pump/probe has been extended to molecules, and it has been used to estimate new detection limits for various species of importance to combustion. In practice, we typically use 2 ps or 60 ps pulses, an interaction for which the rate equation limit is not entirely appropriate. The bulk of this paper describes a new non-perturbative density matrix model that more exactly describes the pump/probe interaction and briefly compares it to the rate equation formalism.

Introduction

We have demonstrated in previous work¹ that picosecond pump/probe is a combustion diagnostic offering an absolute determination of number density. In the rate equation limit, the measurement does not require calibrations or corrections². It is, essentially, a spatially resolved absorption measurement. Even molecules with poor fluorescence yield can be observed with pump/probe. We expect that pump/probe measurements will be insensitive to the collisional environment, because it's possible to make the measurement in time scales much smaller than normal collisional times. Moreover, the transform-limited bandwidth of picosecond pulses is broader than single linewidths, so pressure effects on linewidth do not propagate to the signal.

For a laser source, we prefer to use mode-locked cw lasers because cw laser diagnostics are capable of

recovering all the relevant frequency spectrum information in turbulent flames, power spectral densities (psd's) for example. Psd's require up to 10 kHz bandwidth. Cw lasers also allow continuous monitoring of rapid events, such as ignition. It is important to note, however, that the overall instrumentation bandwidth is controlled somewhat by the detection limits required of the measurement. Pump/probe is a linear technique that scales with pump pulse energy, so the detection limit can be lowered with amplification. The pulses emitted by a mode-locked Ti:sapphire laser oscillator have energy on the order of 20 nJ at the peak of the fundamental (giving peak power in the kilowatt regime). With amplification, pulse energies can reach 0.01 mJ at 50 kHz, and 1 mJ at 1 kHz. While amplification can reduce the instrumentation bandwidth, it provides significant pulse energy, and this is a trade-off that must be considered.

In what follows, we briefly describe a rate equation model for pump/probe as it would be applied to molecules, and we quote expected detection limits for CH, as one example. The rate equations are not fully appropriate for a picosecond interaction, so we describe the development of a non-perturbative, 2-level density matrix model for the pump/probe interaction. Here we, include a discussion of the numerical approach used. We then present some results of the model and briefly compare it to rate equation results for the potassium atom. We then conclude by discussing future directions.

Pump/Probe

In Pump/Probe spectroscopy, the output from the laser is tuned to a transition of interest and the beam is split into two portions. The pump beam (typically much stronger) is directed through a modulator, and is crossed with the probe beam (typically much weaker) in the

flame. This beam crossing forms a sample volume within the flame (see Fig. 1). The pump modulation is impressed upon the resonant molecules in the sample volume because the populations of the ground and excited state are modified by the presence of the pump beam. These populations then modulate the probe beam at the intersection via absorption and stimulated emission, changing the probe irradiance at the modulation rate. This change in irradiance is defined as the modulation depth, expressed as a fraction of the total probe irradiance. After the flame, the pump beam reaches a beam stop, and the probe beam is detected. The detector signal is then synchronously demodulated using a lock-in amplifier. The measured probe modulation depth is proportional to the concentration of molecules. For optically thin conditions, the modulation depth will be at most a few percent. Nevertheless, for mode-locked lasers³, the minimum detectable modulation depth is approximately 10^{-8} .

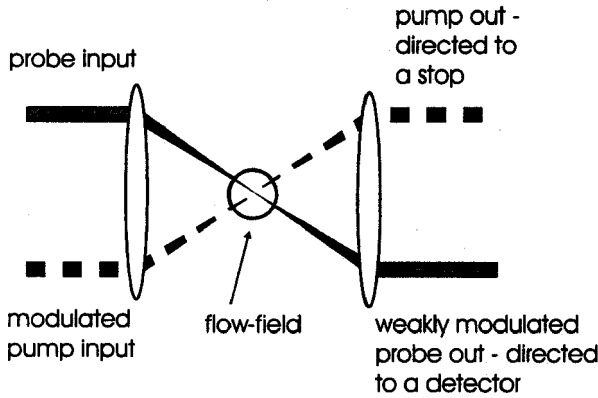


Figure 1. Schematic of single-point Pump/Probe interaction in the flow-field.

We use a Spectra-Physics regeneratively mode-locked Ti:sapphire laser, equipped with both a 2 ps and a 60 ps Gires-Tournois interferometer (Kafka *et al.*, 1992). This laser produces about 1.8 W of output when pumped with 8 W from an intra-cavity doubled, diode-pumped Nd:YVO₄ laser, with autocorrelation pulse-widths around 1.4 ps in the 2 ps configuration. The transform-limited bandwidth is about 0.2 nm. This radiation can then be frequency doubled in 6 mm of LBO to give up to 500 mW of 400 nm radiation. The laser wavelength is monitored several ways: first the laser is tuned using a Burleigh WA 4500 wavemeter, then the flame is ignited and we observe fluorescence. Finally, when signals had been established, the laser is tuned to maximize the signal.

Rate Equation Models

In the interest of preserving space for a discussion of the density matrix model, we discuss rate equation models only briefly. Further details can be found in the work by Fiechtner *et al.*² and by Settersten and Linne⁴.

In our experiments, both the pump and probe are in resonance with the same transition. For a two-level atom, the rate equations then give a modulation depth described by²:

$$\alpha_{MOD} = \left(\ln \left(\frac{1}{\sqrt{2}-1} \right) \right)^2 \frac{c^4 P_{AVE}^{PUMP} N_T L}{16\pi^3 D^2 h f^L (\Delta \nu_{1/2}^L)^2} \cdot \left[\frac{A_{21}^2}{\nu_{12}^5} \frac{g_2}{g_1} \left(1 + \frac{g_2}{g_1} \right) \right] \quad (1)$$

where :

- g_i = degeneracy of level $i = 1$ or 2 ,
- D = focal diameter,
- L = beam interaction length,
- f^L = laser repetition rate,
- ν_{12} = transition frequency,
- $\Delta \nu_{1/2}^L$ = laser bandwidth,
- P_{AVE}^{PUMP} = average power of the pump beam,
- A_{21} = Einstein coefficient for spontaneous emission,
- N_T = absolute number density of absorber.

Here the modulation resides on a large intensity carrier (typically 10^4 to 10^7 larger than the modulated portion of the signal). The model assumes an optically thin analyte, the linear absorption regime, a 2-level system, a temporal top-hat pulse profile and broad bandwidth with respect to the absorption linewidth. The modulation depth (α_{MOD}) is easy to measure, and this is related directly to the number density (N_T). The other terms in equation (1) are usually known or can be measured.

We have demonstrated that Pump/Probe is an absolute determination of number density when this equation was applied to our Potassium measurements and then compared to atomic absorption spectroscopy using a Tungsten filament lamp¹.

Equation (1) represents several approximations, and applies only to a 2-level spectroscopic system. It's easy to use the equation, however, to infer the effect of variables (e.g. pump pulse energy) on the signal, and this is the real utility of the expression. We have recently developed an extended rate equation model for a molecular pump/probe interaction by accounting for numerous ro/vibrational levels, including: the individual Boltzmann fractions, Einstein rate constants for each

line, line broadening and overlap between the laser linewidth and the individual lines pumped by the laser. It was simply assumed that the interaction could be represented by a summation over a number of distinct 2-level resonances. In doing so, the term in square braces in equation (1) becomes:

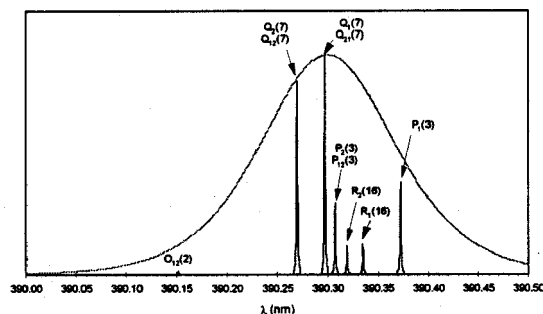
$$\left[\sum_i A_{21,i}^2 \lambda_{21,i}^5 f_{\text{Boltzmann},i} \eta_i \frac{g_{2,i}}{g_{1,i}} \left(1 + \frac{g_{2,i}}{g_{1,i}} \right) \right] \quad (2)$$

The two additional terms in this expression are the Boltzmann fraction $f_{\text{Boltzmann},i}$ and an laser interaction efficiency η_i . The laser interaction efficiency simply has the form of the normalized laser spectral profile. Resonance lines that do not fall on line center will have $\eta < 1$. We assume that energy re-distribution within the upper manifold is negligible within the 10 ps time frame spanning the pump and probe interactions. As before, we assume a top-hat temporal pulse profile. We use the model to computationally tune the laser and maximize the P/P signal. The current optics set in our Ti:sapphire oscillator will allow us to reach the CH B \rightarrow X electronic transition, which is of particular interest to us. The tuning shown in Figure 2 maximizes the pump/probe signal for the B \rightarrow X electronic transition, for a 2 ps and 60 ps pulse. Further details can be found in the work of Settersten and Linne⁵. That work makes extensive use of the spectroscopic data of Luque and Crosley^{6,7,8} and Zachwieja⁹.

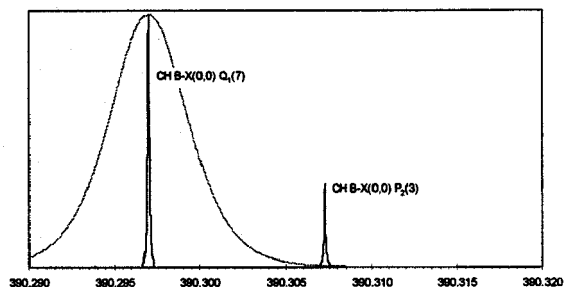
The model just described, when used with conservative numbers (e.g. we assume 200 mW average pump power at about 400 nm when we have routinely reached 300 mW at the experiment), indicates that we can achieve the detection limits contained in Table 1, where the detection limit is written in terms of the following:

$$N \text{ (lower limit)} = \beta \times \alpha_{\text{MOD}} \text{ (lower limit)}.$$

We write it this way because the limit of detection is clearly linked to the lowest modulation depth detectable by the electronics. To detect peak levels of CH in a 2500 K CH₄-O₂ flame (roughly 10^{14} cm^{-3}), our current pump/probe detection system (for the CH B \rightarrow X transition and a 2 ps pulse) must see a signal level of 5×10^{-7} . CH has many energy levels at about the same term value, which produces fairly low Boltzmann fractions for individual lines, and this is the major limitation. Our former Ar:Ion laser pumped Ti:sapphire system generated unusually large amounts of 1/f noise in the probe beam. When this was coupled with a mechanical chopper (at 4 kHz), a modulation depth of 10^{-7} was impossible to measure. These issues lead us to



a.



b.

Figure 2. Example : a. Overlap between part of the CH B \rightarrow X (0,0) band (mixed P,Q & R-branch lines) and the laser emission linewidth at 2 ps - this laser tuning gives maximum P/P signal, b. Similar overlap for 60 ps.

Table 1

Estimated Detection Limits for Standard Pump/Probe

Molecule/Transition	λ (nm)	$\beta \text{ (cm}^{-3}\text{)}$	pulsewidth(ps)
CH B \rightarrow X	390.29	5.0×10^{-21}	2
CH B \rightarrow X	390.30	2.0×10^{-19}	60
CH A \rightarrow X	431.24	5.0×10^{-21}	2
CH A \rightarrow X	430.98	1.2×10^{-19}	60

The following parameters were used : average cw laser power = 200 mW, laser rep rate = 82 MHz, beam focus diam. = 100 μm , interaction length = 100 μm , laser bandwidth = $3.15 \times 10^{11} \text{ Hz} \rightarrow 0.16 \text{ nm}$ (at 390 nm).

investigate the 60 ps case. For the 60 ps case, we would need to reach 2×10^{-5} modulation depth (a routine measurement) if the same average power were available. Unfortunately, doubling efficiency falls rapidly as one goes to 60 ps in the fundamental, where we achieve only a few mW in the blue, increasing the detection limit by the ratio of power levels.

We can improve the basic cw experiment in a straightforward way. We are currently installing a 10 W intra-cavity doubled, diode-pumped Nd:YVO₄ pump laser. This will reduce the noise in the Ti:sapphire significantly. The manufacturer's data show an order of

magnitude lower noise for this pump laser when compared to a properly operating Ar:Ion laser. This new laser system will be used with an E/O modulator and lock-in extender (both operating at > 100 kHz, beyond the $1/f$ noise spectrum for this laser). It is not clear at this point what lower limit of modulation we can reach with this system. Work continues in this 82 MHz regime, but amplifiers are another approach for reducing the detection limit.

Wright Laboratories has recently installed a 50 kHz Ti:sapphire regenerative amplifier that produces 0.01 mJ/pulse in the red. This will easily give pump energies near 2 μ J/pulse at 2 ps and 400 nm. The values for β in Table 1 will then be decreased by a factor of about 10^2 . In the amplified case, to detect the same peak levels of $\text{CH B} \rightarrow \text{X}$ in the 2500 K $\text{CH}_4\text{-O}_2$ flame at 2 ps, the detection system would need to see a signal level of 10^{-3} , which is trivial.

The group at CSM has recently ordered a complimentary 1 kHz regenerative amplifier, generating 1 mJ in the red. This will easily give pump energies near 200 μ J/pulse at 2 ps and 400 nm. The values for β in Table 1 will then be decreased by a factor of about 10^4 . In the amplified case, to detect the same peak levels of $\text{CH B} \rightarrow \text{X}$ in the 2500 K $\text{CH}_4\text{-O}_2$ flame at 2 ps, the detection system would only need to see a signal level of 1%. Another way to state the same fact is that the detection limit will be reduced by a factor of 10^4 , at the price of instrumentation bandwidth. The group at CSM is interested in using pump/probe for imaging, however, requiring that the pump beam be spread into a sheet. Clearly, extra pump pulse energy is required in order to accomplish this.

Density Matrix Model

As stated in the introduction, we expect that pump/probe measurements will be insensitive to the collisional environment, because it's possible to make the measurement in time scales much smaller than normal collisional times. Our pulsewidths are typically 2 ps long, and the probe pulse is adjusted to trail the pump pulse by only a few pulsewidths. These time frames are significantly shorter than the collision times, coherence lifetimes, and the excited state lifetimes of molecules in flames. This necessarily means that the probe pulse will sample the coherences created by the pump pulse. As such, it is not accurate to use the rate equations to describe the pump/probe interaction.

For this reason, we have developed a non-perturbative model that is based upon semi-classical theory. It combines the time-dependent density matrix equations with Maxwell's equations to describe the propagation of the pump and probe pulses. Our goal is

to discover how well the rate equation model approximates the pump/probe interaction, when it occurs within the rate equation limits, or to find a similarly simple expression. Failing that, we plan to find some other way to relate the experimentally measured modulation depth to number density. We also plan to define the limits of applicability of such expressions, and then to explore other sensing possibilities offered by departures from the rate equation limits.

This model combines three formalisms to self-consistently describe pulse propagation. First, the density matrix formalism of Quantum Mechanics describes the microscopic response of resonant and near-resonant atoms immersed in the laser field. Secondly, Statistical Physics describes how the individual atomic responses add up to produce a net induced polarization on the macroscopic level. This statistical averaging takes into account the Doppler broadening of the resonance. Lastly, from Classical Electrodynamics, we obtain the one-dimensional wave equation that describes the propagation of the laser pulse. Each of these topics will be discussed in three sections to follow. Prior to that, we will set the stage for those sections by introducing the formalism used to represent the laser pulses.

Pulse Representation

The pump and probe pulses will be described as plane waves traveling in the \hat{e}_z -direction with a linear electric field polarization in the \hat{e}_x -direction. The model described here, therefore, does not assume the crossed beam geometry shown in Figure 1, but instead a collinear geometry. The electric field of a pulse can be expressed as the product of a slowly varying envelope function and a rapidly varying phase, both of which are functions of the spatial coordinate z and the time t :

$$\vec{E}(z,t) = \hat{e}_z \mathcal{E}(z,t) \left(e^{-i[\omega_0 t - k_0 z + \phi(z,t)]} + c.c. \right) \quad (3).$$

Both the angular frequency ω_0 and the propagation constant k_0 are considered constants, while the slowly varying phase term $\phi(z,t)$ allows for dispersive effects. With no loss of generality, $\phi(z,t)$ can be incorporated into the envelope function, resulting in a complex envelope function with real and imaginary components \mathcal{E}^R and \mathcal{E}^I :

$$\vec{E}(z,t) = \hat{e}_z \left(\tilde{\mathcal{E}}(z,t) e^{-i[\omega_0 t - k_0 z]} + c.c. \right) \quad (4).$$

This transformation allows us to describe the propagation of a pulse solely in terms of the propagation of a complex envelope since the rapidly varying phase term cannot change form. We describe the net induced polarization of the sample in an analogous way:

$$\bar{P}(z,t) = \hat{e}_z \left(\tilde{p}(z,t) e^{-i[\omega_o t - k_o z]} + c.c. \right) \quad (5).$$

Since the pump and probe pulses are produced from the same laser by using a beam splitter, their envelope functions have the same functional form with the same initial phase ϕ , but they can have different magnitudes. Also, when describing both pulses in the same coordinate system, a spatial transformation must be applied to the probe pulse. This is due to the fact that the pump and probe pulses travel through different pathlengths on their way to the interaction volume. If the probe pathlength is a distance Δz longer than that of the pump, the necessary spatial transform is $z \rightarrow z + \Delta z$. Since the beams are collinear through the interaction volume, the superposition principle can be used to describe the total field due to both pulses. Assuming that both pulses have the same electric field polarization, the total electric field is equal to the sum of the two fields. If the pump and probe pulses are each expressed as in equation (3), the total electric field takes the form of Equation (4) where the real and imaginary parts of the total envelope function are given by the following expressions.

$$\begin{aligned} \varepsilon^R(z,t) &= \varepsilon_1(z,t) \cos \phi \\ &+ \varepsilon_2(z + \Delta z, t) \left[\begin{array}{l} \cos \phi \cos k_o \Delta z \\ + \sin \phi \sin k_o \Delta z \end{array} \right] \end{aligned} \quad (6a)$$

$$\begin{aligned} \varepsilon^I(z,t) &= -\varepsilon_1(z,t) \sin \phi \\ &+ \varepsilon_2(z + \Delta z, t) \left[\begin{array}{l} \cos \phi \sin k_o \Delta z \\ - \sin \phi \cos k_o \Delta z \end{array} \right] \end{aligned} \quad (6b)$$

An example of an envelope function used to describe a pump and a probe pulse in this manner is shown in Figure 6 in the “Results” section.

Density Matrix Equations

We use the density matrix formalism to describe the response of resonant or near-resonant atoms to the electric field of a laser pulse. Definition of the density matrix, discussion of its properties, and derivations of the density matrix equations are found in most graduate quantum mechanics texts¹⁰. Additionally, we have found several books that contain useful introductions to this formalism with particular emphasis on laser-matter interaction^{11,12,13}.

For the purposes of this study, we will model a resonant atom or molecule as a closed two-level system. This simplification can be justified in cases where the resonance is isolated and where transfer rates between

the resonant energy levels and other energy levels are negligible on the time scales considered by the model.

The two-level system that will be considered is shown in Figure 3. The combined spontaneous emission and collisional de-excitation rates are given by Γ_{21} . The collisional dephasing rate γ_{21} accounts for collisional broadening. Collisional excitation rates are considered negligible.

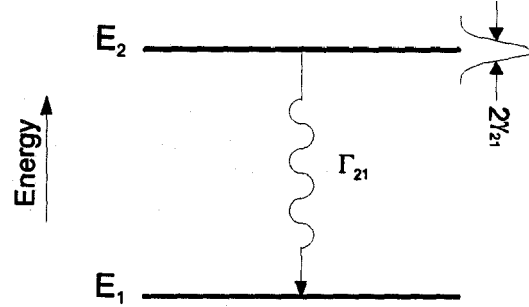


Figure 3. Energy level diagram for a closed two-level system. Also depicted in the figure are collisional/radiative de-excitation (with a rate Γ_{21}), and collisional broadening (characterized by the coherence dephasing rate γ_{21}).

The density matrix ρ for an atom contains all necessary information about this quantum system. For a two-level atom, the diagonal elements ρ_{11} and ρ_{22} are the probabilities that the atom is in state 1 or 2, respectively. For a closed two-level system, the trace of the density matrix must be equal to one, since the atom must be in one state or the other. The off-diagonal elements are the coherences between the states with the property that $\rho_{21} = \rho_{12}^*$.

When a resonant electric field is applied to an atom, the interaction Hamiltonian, denoted by V , is introduced into the Schrödinger equation. In the electric dipole approximation, the off-diagonal elements of the interaction Hamiltonian are given by:

$$\begin{aligned} V_{21}(t) &= -\mu_{21} E(t) \\ V_{12}(t) &= -\mu_{12} E(t) \end{aligned} \quad (7).$$

In general, the off-diagonal elements are complex conjugates. However, the dipole matrix elements μ_{12} and μ_{21} can be made purely real and equal, with no loss of generality, if the basis vectors describing the energy eigenstates 1 and 2 are judiciously chosen. In that case, the interaction Hamiltonian is also purely real, and $V_{21} = V_{12}$.

The density matrix equations are a set of coupled ordinary differential equations that describe the time evolution of the density matrix elements in response to an interaction Hamiltonian. With the relaxation rates defined earlier, the density matrix equations for a 2-level system are given by¹²:

$$\frac{d}{dt} \rho_{11} = \Gamma_{21} \rho_{22} + \frac{i}{\hbar} (V_{21} \rho_{12} - \rho_{21} V_{12}) \quad (8a),$$

$$\frac{d}{dt} \rho_{21} = -(i\omega_{21} + \gamma_{21}) \rho_{21} + \frac{i}{\hbar} V_{21} (\rho_{22} - \rho_{11}) \quad (8b).$$

When the laser electric field is applied, the system responds at the optical frequency ω_o . As such, it stands to reason that the coherence can be written in terms of the product of a slowly varying complex envelope and the same rapidly varying phase term, as in equation (4):

$$\rho_{21} = \tilde{\sigma}_{21} e^{-i(\omega_o t - k_o z)} \quad (9).$$

The envelope function for the coherence has real and imaginary parts σ_{21}^R and σ_{21}^I , respectively.

When the interaction Hamiltonian is expressed explicitly, and equation (9) is substituted into the differential equations (8a) and (8b), the following two equations result:

$$\frac{d}{dt} \rho_{11} = \Gamma_{21} \rho_{22} + \frac{i\mu_{21}}{\hbar} \left(\begin{array}{c} -\tilde{\varepsilon} \tilde{\sigma}_{21}^* + \tilde{\varepsilon}^* \tilde{\sigma}_{21} \\ \tilde{\varepsilon} \tilde{\sigma}_{21} e^{-2i(\omega_o t - k_o z)} \\ -c.c. \end{array} \right) \quad (10a),$$

$$\frac{d}{dt} \tilde{\sigma}_{21} = -[i(\omega_{21} - \omega_o) + \gamma_{21}] \tilde{\sigma}_{21} - \frac{i\mu_{21}}{\hbar} (\rho_{22} - \rho_{11}) (\tilde{\varepsilon} + \tilde{\varepsilon}^* e^{2i(\omega_o t - k_o z)}) \quad (10b).$$

Both of these equations have terms that are slowly varying and terms that oscillate at twice the optical frequency ω_o . In the rotating wave approximation, the rapidly varying terms are neglected. Furthermore, these equations can be expressed in terms of the complex and real parts of the envelope functions for the electric field and for the coherences. This results in three real equations:

$$\frac{d}{dt} \rho_{11} = \Gamma_{21} (1 - \rho_{11}) + \frac{2\mu_{21}}{\hbar} (\varepsilon^I \sigma_{21}^R - \varepsilon^R \sigma_{21}^I) \quad (11a),$$

$$\begin{aligned} \frac{d}{dt} \sigma_{21}^R &= -\gamma_{21} \sigma_{21}^R + (\omega_{21} - \omega_o) \sigma_{21}^I \\ &+ \frac{\mu_{21}}{\hbar} \varepsilon^I (1 - 2\rho_{11}) \end{aligned} \quad (11b),$$

$$\begin{aligned} \frac{d}{dt} \sigma_{21}^I &= -\gamma_{21} \sigma_{21}^I - (\omega_{21} - \omega_o) \sigma_{21}^R \\ &- \frac{\mu_{21}}{\hbar} \varepsilon^R (1 - 2\rho_{11}) \end{aligned} \quad (11c).$$

Given an initial electric field envelope function (ε), these three equations can be directly integrated to produce the time evolution of the coherence.

The coherence is then used to calculate the atomic response, given by the expectation value of the atomic dipole moment. Using the formalism of Quantum Mechanics, the expectation value of any operator is given by the trace of the matrix resulting from the density matrix acting on the operator. For the dipole moment operator, which has non-zero elements only off-diagonal, the expectation value is simply:

$$\begin{aligned} \langle \mu \rangle &= \rho_{12} \mu_{21} + \rho_{21} \mu_{12} \\ &= \mu_{21} (\tilde{\sigma}_{21} e^{-i(\omega_o t - k_o z)} + c.c.) \end{aligned} \quad (12).$$

Statistical Averaging

The net induced polarization is a macroscopic property that results from the sum of the microscopic responses of individual atoms, given by equation (12). The macroscopic polarization in a volume V is the volume average of the atomic dipole moments of all M atoms in V :

$$P(z, t) = \frac{1}{V} \sum_{i=1}^M \langle \mu \rangle_i \quad (13).$$

The atomic dipole moments in this problem can be parameterized by the atomic velocity component u along the optical axis \hat{e}_z . Atoms traveling with different velocities along that axis will respond to the laser excitation at an optical frequency that is Doppler shifted. With this in mind, we introduce a more explicit notation that emphasizes this parameterization. A partial polarization $P(z, t; u)$ is defined as the time-dependent expectation value of the dipole moment of an atom at position z with a velocity component u :

$$P(z, t; u) = \langle \mu(z, t; u) \rangle \quad (14).$$

The summation in Equation (13) is treated in statistical physics by introduction of the velocity distribution function. For this analysis, we consider a

steady-state and spatially-uniform Maxwellian velocity distribution, which is only a function of the velocity component u . In this case, the probability that an atom has a velocity component u in the interval $(u, u+du)$ is given by:

$$f(u)du = \left(\frac{m}{2\pi k_B T} \right)^{\frac{1}{2}} e^{-\frac{mu^2}{2k_B T}} du \quad (15),$$

where:

m	=	Mass of Atom,
k_B	=	Boltzmann Constant,
T	=	Translational Temperature.

Using this distribution function, Equation (13) becomes the following integral, where N_{TOT} is the total number density of the resonant atomic species:

$$P(z,t) = N_{TOT} \int_{-\infty}^{+\infty} P(z,t;u) f(u) du \quad (16).$$

The partial polarization can be written in terms of the coherence envelope function. In the notation of Equation (5), the envelope function for the net polarization is:

$$\tilde{p}(z,t) = N_{TOT} \mu_{21} \int_{-\infty}^{+\infty} \tilde{\sigma}_{21}(z,t;u) f(u) du \quad (17).$$

One-Dimensional Wave Equation

The one-dimensional wave equation is derived from Maxwell's Equations, and it has the following form in MKS units (to switch to Gaussian (CGS) units, simply replace $1/\epsilon_0$ with 4π):

$$\left[\frac{\partial^2}{\partial z^2} - \frac{1}{c^2} \frac{\partial^2}{\partial t^2} \right] E(z,t) = \frac{1}{\epsilon_0 c^2} \frac{\partial^2}{\partial t^2} P(z,t) \quad (18).$$

It is desirable to reduce the second order wave equation to a first order differential equation. This reduction is possible using an important approximation and a small bit of algebra. First, equations (4) and (5) are substituted into the wave equation. Next, invoking the slowly varying envelope approximation (SVEA), second order derivatives of the slowly varying functions $\mathcal{E}(z,t)$ and $p(z,t)$ are neglected. Furthermore, time derivatives of $p(z,t)$ can also be ignored with respect to the other terms in the equation. Finally, writing the wave equation in terms of the real and imaginary parts of the envelope functions, the following two real differential equations result for terms that are in phase and in quadrature with the optical phase:

$$\left[\frac{\partial}{\partial z} + \frac{1}{c} \frac{\partial}{\partial t} \right] \mathcal{E}^R(z,t) = -\frac{k_0}{2\epsilon_0} P^I(z,t) \quad (19a),$$

$$\left[\frac{\partial}{\partial z} + \frac{1}{c} \frac{\partial}{\partial t} \right] \mathcal{E}^I(z,t) = \frac{k_0}{2\epsilon_0} P^R(z,t) \quad (19b).$$

A further simplification results by invoking the retarded time transformation: $t \rightarrow \tau = t - z/c$. This change of variables transforms the wave equations from partial differential equations to two ordinary differential equations that can be directly numerically integrated:

$$\frac{\partial}{\partial z} \mathcal{E}^R(z,\tau) = -\frac{k_0}{2\epsilon_0} P^I(z,\tau) \quad (20a),$$

$$\frac{\partial}{\partial z} \mathcal{E}^I(z,\tau) = \frac{k_0}{2\epsilon_0} P^R(z,\tau) \quad (20b).$$

Pump/Probe Model

The complete model employs a quantum-mechanically-correct description of the interaction of intense laser pulses with resonant or near-resonant two-level atoms. The resulting density matrix equations characterize the individual atomic responses to the applied laser field for atoms at a particular position in space and with a particular velocity component along the optical axis. Assuming a Maxwellian velocity distribution for the target atoms, the individual atomic responses are statistically averaged, resulting in the net induced polarization at that position. The induced polarization determines how the laser pulse propagates in space according to the one-dimensional wave equation. The model invokes the slowly varying envelope approximation (SVEA) and the rotating wave approximation (RWA) to reduce the description to a set of three coupled ordinary differential equations (ODE) in time and two ODE's in space. The input field envelope is defined such that it includes both the pump and probe pulses, and the model calculates the attenuation/gain of the envelope as the pulses propagate through the sample volume.

The five differential equations describing this system are given in equations (11) and (20). These are repeated below using explicit notation for the dependencies of the variables:

$$\begin{aligned} \frac{\partial}{\partial \tau} \rho_{11}(z,\tau;u) &= \Gamma_{21} [1 - \rho_{11}(z,\tau;u)] \\ &+ \frac{2\mu_{21}}{\hbar} \left[\mathcal{E}^I(z,\tau) \sigma_{21}^R(z,\tau;u) \right. \\ &\quad \left. - \mathcal{E}^R(z,\tau) \sigma_{21}^I(z,\tau;u) \right] \end{aligned} \quad (21a),$$

$$\begin{aligned} \frac{\partial}{\partial \tau} \sigma_{21}^R(z, \tau; u) &= -\gamma_{21} \sigma_{21}^R(z, \tau; u) \\ &+ [\omega_{21} - \omega(u)] \sigma_{21}^I(z, \tau; u) \\ &+ \frac{\mu_{21}}{\hbar} \mathcal{E}^I(z, \tau) [1 - 2\rho_{11}(z, \tau; u)] \end{aligned} \quad (21b),$$

$$\begin{aligned} \frac{\partial}{\partial \tau} \sigma_{21}^I(z, \tau; u) &= -\gamma_{21} \sigma_{21}^I(z, \tau; u) \\ &- [\omega_{21} - \omega(u)] \sigma_{21}^R(z, \tau; u) \\ &- \frac{\mu_{21}}{\hbar} \mathcal{E}^R(z, \tau) [1 - 2\rho_{11}(z, \tau; u)] \end{aligned} \quad (21c),$$

$$\frac{\partial}{\partial z} \mathcal{E}^R(z, \tau) = -\frac{k_o}{2\epsilon_o} P^I(z, \tau) \quad (21d),$$

$$\frac{\partial}{\partial z} \mathcal{E}^I(z, \tau) = \frac{k_o}{2\epsilon_o} P^R(z, \tau) \quad (21e).$$

The first three differential equations describe the time evolution of the density matrix at a particular spatial location for an atom with a particular velocity component. The atoms addressed by these equations will see a Doppler shifted laser frequency, and as such, the apparent laser frequency ω is shown to have a velocity dependence. The Doppler-shifted frequency is:

$$\omega(u) = \omega_o - k_o u \quad (22).$$

The last two differential equations relate the spatial gradient of the electric field to the induced polarization. The induced polarization envelope functions are directly related to the coherence envelope functions as follows:

$$\begin{aligned} P^R(z, \tau) &= N_{\text{TOT}} \mu_{21} \left(\frac{m}{2\pi k_B T} \right)^{\frac{1}{2}} \\ &\bullet \int_{-\infty}^{+\infty} \sigma_{21}^R(z, \tau; u) e^{-\frac{mu^2}{2k_B T}} du \end{aligned} \quad (23a),$$

$$\begin{aligned} P^I(z, \tau) &= N_{\text{TOT}} \mu_{21} \left(\frac{m}{2\pi k_B T} \right)^{\frac{1}{2}} \\ &\bullet \int_{-\infty}^{+\infty} \sigma_{21}^I(z, \tau; u) e^{-\frac{mu^2}{2k_B T}} du \end{aligned} \quad (23b).$$

Numerical Solution

In order to numerically solve these equations, a spatial-temporal grid is set up as shown in Figure 4.

The interaction volume starts at $z_1=0$, and it is discretized into I positions with a uniform spacing h_z . At each position z_i , the electric field is solved on a temporal grid that starts at the retarded time $\tau_1=0$, ends at time τ_j , and has a uniform spacing h_τ . At each position, the atomic response is calculated for velocity groups u_k where $k=1,2,\dots,K$.

We assume that prior to the interaction region ($z \leq 0$), the electric field has not had any resonant interactions with matter. The electric field envelope is assigned a particular functional form that depends upon experimental conditions such as the laser power, the beam splitter ratio, and the pump-probe pulse delay. The electric field is then specified on the τ -axis as shown in Figure 4. To indicate that the values of the electric field envelopes are known at these grid points, the left side of each grid point is blackened.

We define the electric field to be zero for $\tau \leq 0$ at $z=0$. Since information cannot travel faster than the speed of light, this constraint forces the electric field to be zero for $\tau \leq 0$ at all z . Therefore, the resonant atoms are at equilibrium for these conditions, and the density matrix assumes equilibrium values at grid points along the z -axis in Figure 4. To indicate that the values of the density matrix elements, and therefore, the polarization envelope functions, are known at these grid points, the right half of each has been blackened.

The density matrix equations (21a-c), form a set of coupled ODE's at a position z_i . If the values of the electric field envelope functions are known for all τ_j at z_i , and the density matrix elements are known for $\tau=0$ at z_i , this set of ODE's takes the form of an initial value problem (IVP). In other words, the equations can be directly integrated by marching forward in time from $\tau=0$. This is the case for the τ -axis in Figure 4. A rectangle has been drawn around these grid points to indicate that the density matrix equations can be solved for these points when the initial conditions are specified. The integration is performed using a Bulirsch-Stoer adaptive step-sizing routine¹⁵. This integrator solves for ρ_{11} , σ_{21}^R , and σ_{21}^I at each time grid point. However, since it is an adaptively stepping algorithm, it requires

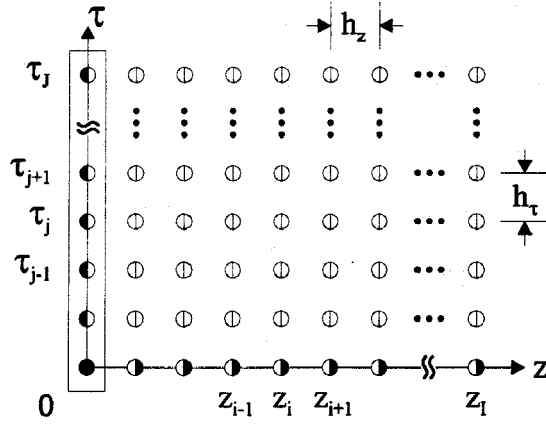


Figure 4. The spatial-temporal grid on which the pulse propagation equations are solved. The state shown in the figure corresponds to initial conditions. A circle with the right half blackened indicates that the values of p^R and p^I are known at that grid point. A darkened left half indicates that the values of ϵ^R and ϵ^I are known.

values of ϵ^R and ϵ^I between the grid points. When such an evaluation is necessary, cubic spline interpolation is used.

To obtain the induced polarization envelope functions at position z_i , the density matrix equations must be solved for each velocity group, u_k . The results are averaged at each grid point as specified by the integrals in equations (23a) and (23b). These integrals have the form of $g(x)\exp(-x^2)dx$, and as such, they are efficiently computed using Gauss-Hermite integration¹⁵. For a K^{th} -order Gauss-Hermite integration, the values of u_k are chosen so that they correspond to the zeros of the K^{th} -order Hermitian polynomial x_k :

$$u_k = \sqrt{\frac{2k_B T}{m}} x_k ; \quad k = 1..K \quad (24).$$

Using weight functions w_k , defined in reference [15], the integrals are approximated as follows:

$$\begin{aligned} & \int_{-\infty}^{+\infty} \sigma_{21}(z_i, \tau_j; u) e^{-\frac{mu^2}{2k_B T}} du \\ & \approx \frac{1}{\sqrt{\pi}} \sum_{k=1}^K \sigma_{21}(z_i, \tau_j; u_k) w_k \end{aligned} \quad (25)$$

After these integrals have been computed for all τ_j at z_1 , both the electric field and the induced polarization are known at z_1 . This state is shown in Figure 5a, where the grid points along the τ -axis are completely filled-in.

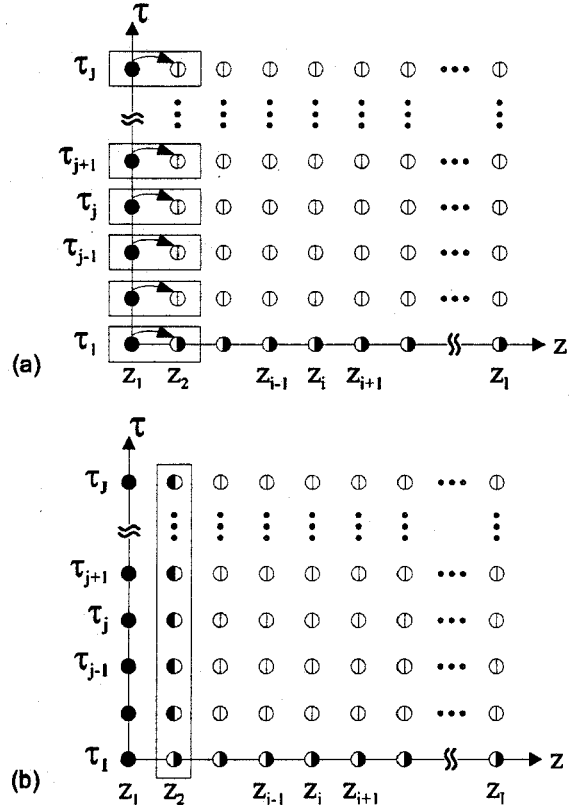


Figure 5. (a) Euler method is used to compute ϵ^R and ϵ^I at z_2 . (b) The induced polarization envelopes, $p^R(z_2, \tau_j)$ and $p^I(z_2, \tau_j)$, are calculated by integrating the density matrix equations and statistical averaging the atomic responses at z_2 .

The propagation of the electric field is determined by equations (21d-e). These equations are numerically integrated between z_1 and z_2 using the simple Euler method at each time τ_j . These steps are symbolically shown in Figure 5a. The 2J equations used to compute the electric field envelope functions are:

$$\epsilon^R(z_2, \tau_j) = -h_z \left[\frac{k_0}{2\epsilon_0} p^I(z_1, \tau_j) \right] ; \quad j = 1..J \quad (26a),$$

$$\epsilon^I(z_2, \tau_j) = h_z \left[\frac{k_0}{2\epsilon_0} p^R(z_1, \tau_j) \right] ; \quad j = 1..J \quad (26b).$$

As a result of these integrations, all of the initial conditions necessary to integrate the density matrix equations at position z_2 are now known. By integrating equations (21a-c) for each of the K velocity groups, and statistically averaging the atomic responses at each time as dictated by equation (25), the induced polarization at z_2 is calculated. This step involves the grid points within the rectangle in Figure 5b.

At this point, values of the electric field and induced polarization envelopes are known for all τ_j at the first two positions. With this information, a simple predictor-corrector scheme is used to calculate the electric field envelopes at the next position. For each time τ_j , prediction of the electric field envelope functions are made by taking symmetric Euler steps from z_0 to z_2 using the value of the polarization at the central grid point. In general, the predictor step is given below, where the subscript “p” on the electric field denotes a *predicted* value.

$$\begin{aligned} \varepsilon_p^R(z_{i+1}, \tau_j) &= \varepsilon^R(z_{i-1}, \tau_j) \\ &- 2h_z \left[\frac{k_0}{2\varepsilon_0} p^I(z_i, \tau_j) \right]; j = 1..J \end{aligned} \quad (27a)$$

$$\begin{aligned} \varepsilon_p^I(z_{i+1}, \tau_j) &= \varepsilon^I(z_{i-1}, \tau_j) \\ &+ 2h_z \left[\frac{k_0}{2\varepsilon_0} p^R(z_i, \tau_j) \right]; j = 1..J \end{aligned} \quad (27b)$$

The density matrix equations and statistical summations are computed at position z_{i+1} using the predicted values of the electric field. This results in predicted values of the polarization at z_{i+1} . Finally, corrected values for the electric field at z_{i+1} are computed by taking an Euler step from z_i to z_{i+1} using the average of the polarization at z_i and the predicted polarization at z_{i+1} . The *corrector* step is given by the following equations:

$$\begin{aligned} \varepsilon^R(z_{i+1}, \tau_j) &= \varepsilon^R(z_i, \tau_j) \\ &- \frac{1}{2} h_z \frac{k_0}{2\varepsilon_0} \left[p^I(z_i, \tau_j) + p_p^I(z_{i+1}, \tau_j) \right]; j = 1..J \end{aligned} \quad (28a)$$

$$\begin{aligned} \varepsilon^I(z_{i+1}, \tau_j) &= \varepsilon^I(z_i, \tau_j) \\ &+ \frac{1}{2} h_z \frac{k_0}{2\varepsilon_0} \left[p^R(z_i, \tau_j) + p_p^R(z_{i+1}, \tau_j) \right]; j = 1..J \end{aligned} \quad (28b)$$

After each corrector step, the integral of the square of the electric field envelope is computed using Romberg integration¹⁵. Like the Bulirsch-Stoer algorithm, this is an extrapolative method that requires function evaluation between grid points. Once again, cubic spline interpolation is used for these evaluations. The limits of integration are set to contain only the probe pulse so that the result is proportional to the total probe pulse energy. By normalizing this result to that for position z_1 , one obtains the pulse-averaged probe attenuation at position z_i .

Repeating this predictor-corrector scheme, the electric field and induced polarization is determined at all grid points.

Density Matrix Model Results

We now present some preliminary results for pulse propagation in pump/probe experiments with potassium. We are focusing on potassium because we wish to validate our model results experimentally, and we are well-suited to carry out potassium pump/probe experiments. Potassium has several advantages which make it ideal for this characterization. First, it has two strong ground state transitions in the fundamental tuning range of Ti:Sapphire. Secondly, for these resonances, potassium is completely described by a three-level model. Therefore, we can be certain that our model accurately describes the physical interaction. Although our current model uses the two-level density matrix equations, we will implement a three-level model soon. The following simulations use parameters typical to proposed experimental conditions.

Experimental Parameters

The proposed experiments will employ the Spectra Physics regeneratively mode-locked Ti:Sapphire laser system described earlier. The beam diameter is approximately 100 μm at the sample volume. Assuming a sech^2 intensity profile, the electric field magnitude at the sample is approximately 1.5×10^7 V/m for the 2-ps pulses, and 2.8×10^6 V/m for the 60-ps pulses. The transform-limited spectral FWHM of a 2-ps pulse is $\Delta\omega_{2\text{ps}} = 0.99$ ps^{-1} , while that of a 60-ps pulse is $\Delta\omega_{60\text{ps}} = 3.3 \times 10^{-2}$ ps^{-1} .

The laser will be tuned to the $4^2S_{1/2}$ - $4^2P_{1/2}$ transition of atomic potassium at 769.9 nm. Both the ground state and the excited state have a degeneracy of 2, so the density matrix model does not need to explicitly account for degeneracy of states. Fiechtner and Linne¹ probed the $4^2S_{1/2}$ - $4^2P_{3/2}$ transition (766.5 nm) in prior pump/probe experiments, but to properly model that transition, the density matrix equations would need to explicitly account for the different degeneracies of the two states. For the conditions of their experiments, it was determined that to avoid saturation the pump and probe beam powers had to be kept below 4 mW (49 pJ per pulse) and 5 mW (61 pJ/pulse), respectively¹⁶.

The spontaneous emission coefficient for the $4^2S_{1/2}$ - $4^2P_{1/2}$ transition¹⁷ is approximately 0.382×10^8 s^{-1} . This value corresponds to a dipole moment of 2.5×10^{-29} C·m. For atmospheric flame conditions, we assume that the collisional dephasing rate γ_{21} and the de-excitation rate Γ_{21} are both equal to 5×10^9 s^{-1} .

A Winefordner-style aspirating burner will be used to seed the potassium into an atmospheric methane/air flame. We assume an equilibrium temperature of approximately 2000 K, which corresponds to a FWHM

of the potassium velocity distribution of 922 m/s. The corresponding Doppler broadening of the atomic line is $\Delta\omega_{\text{Doppler}} = 7.5 \times 10^{-3} \text{ ps}^{-1}$.

For simulations involving 2-ps pulses, the temporal discretization is typically set to 0.05 ps so that 40 grid points span one intensity FWHM. All simulations shown here use 2 mm interaction region, and the spatial discretization is chosen so that the difference between the predictor (27) and the corrector step (28) is kept within a 5% tolerance. When Doppler broadening is explicitly included in the simulations, 19 velocity groups are used in the integrations defined by equation (25).

Initial Conditions

We assume that when unperturbed, all atoms are in the ground state. Furthermore, the coherences must be zero when no coherent excitation is present. These initial conditions are summarized as follows.

$$\left. \begin{aligned} \rho_{11}(z_i, 0; u_k) &= 1 \\ \sigma_{21}^R(z_i, 0; u_k) &= \sigma_{21}^I(z_i, 0; u_k) = 0 \end{aligned} \right\} \quad (28)$$

$$i = 1..I, k = 1..K$$

We further assume that the mode-locked laser pulses are described by hyperbolic secant envelope functions. The envelope function for the pump has a magnitude ε_1 , and it peaks at $\tau = \tau_1$. The probe envelope has a magnitude ε_2 , and it peaks at $\tau = \tau_2$. The pulses are spatially separated by $\Delta z = c(\tau_2 - \tau_1)$. Each pulse has the same intensity full width at half-maximum (FWHM) which is denoted by $\Delta\tau_{\text{FWHM}}$. Using (6), the electric field envelope is specified at $z=0$ by the following two functions.

$$\begin{aligned} \varepsilon^R(0, \tau) &= \varepsilon_1 \operatorname{sech} \left[\frac{-2 \ln(\sqrt{2}-1)}{\Delta\tau_{\text{FWHM}}} (\tau - \tau_1) \right] \cos \varphi \\ &+ \varepsilon_2 \operatorname{sech} \left[\frac{-2 \ln(\sqrt{2}-1)}{\Delta\tau_{\text{FWHM}}} (\tau - \tau_2) \right] \\ &[\cos \varphi \cos k_o \Delta z + \sin \varphi \sin k_o \Delta z] \end{aligned} \quad (30a)$$

$$\begin{aligned} \varepsilon^I(0, \tau) &= -\varepsilon_1 \operatorname{sech} \left[\frac{-2 \ln(\sqrt{2}-1)}{\Delta\tau_{\text{FWHM}}} (\tau - \tau_1) \right] \sin \varphi \\ &+ \varepsilon_2 \operatorname{sech} \left[\frac{-2 \ln(\sqrt{2}-1)}{\Delta\tau_{\text{FWHM}}} (\tau - \tau_2) \right] \\ &[\cos \varphi \sin k_o \Delta z - \sin \varphi \cos k_o \Delta z] \end{aligned} \quad (30b)$$

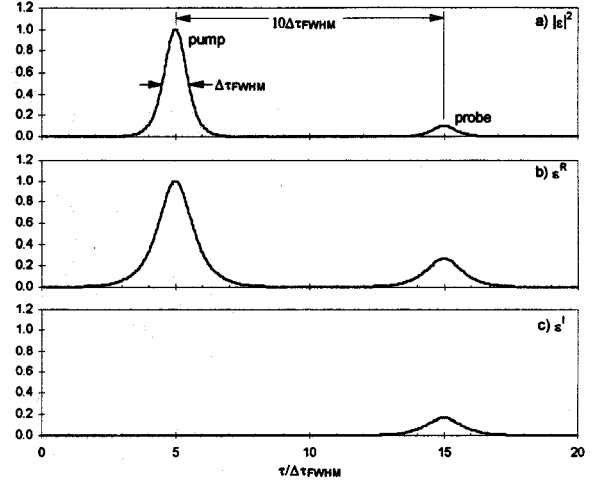


Figure 6. Example of the electric field envelope for $z=0$. The square of the magnitude of the envelope function is shown in part a). Part b) show the real part of the complex envelope function, and part c) shows the imaginary part of the envelope function.

Figure 6a depicts the modulus squared for a pump/probe envelope. In this example, the phase is set so that the pump envelope is purely real at $z=0$ ($\varphi(0, \tau)=0$ in Equation (3)). The probe intensity is 10% of the pump intensity. The peak of the pump pulse occurs at $\tau_1 = 5\Delta\tau_{\text{FWHM}}$, and the probe pulse peaks at $\tau_2 = \tau_1 + 10\Delta\tau_{\text{FWHM}}$. For the numerical integration, it is important to truncate the envelope functions, so that the laser electric field is always zero for $\tau \leq 0$. A further restriction is placed on the functions to distinctly separate the pump and probe pulses. This is accomplished by setting the electric field for each pulse to zero for $|\tau - \tau_{\text{peak}}| > 4\Delta\tau_{\text{FWHM}}$.

Figures 6b) and 6c) show the real and imaginary parts of the envelope function as determined from (30). When considered independently, the pump and probe pulses were taken to be purely real. However, when the envelope function for both pulses is calculated, the imaginary part is non-zero due to the phase $k_o \Delta z$ introduced by the pump-probe delay.

An important point to be made here is that very slight changes in Δz , on the order of a fraction of an optical wavelength, can dramatically change the envelope function. For example, if Δz is set so that the envelope is purely real, coherences due to the pump pulse are exactly in phase with the probe pulse. If Δz is then shifted one-half of an optical wavelength, the pump and probe are exactly out of phase. Shifts of this magnitude will most definitely occur in an experiment. Therefore, future improvements to the model will include handling of these as well as other typical fluctuations.

Doppler Effects

The model includes Doppler effects by averaging atomic responses over a Maxwellian distribution. However, for potassium, under atmospheric flame conditions, Doppler broadening is negligible with respect to the spectral bandwidth of a 2-ps pulse. At 2000 K, the Doppler width for potassium is two orders of magnitude smaller than the laser spectral bandwidth. Therefore, atomic responses vary little for velocity groups within the Maxwellian distribution, and the average atomic response turns out to be the response that is calculated for stationary atoms. Therefore, the remaining simulations do not carry out the statistical average explicitly.

Probe Pulse Propagation - No Pump

The following figure shows the excited state population that results after a single pulse interaction. For these simulations, the pulse is propagated through an interaction length of 2 mm, with a total potassium number density of 10^{11} cm^{-3} .

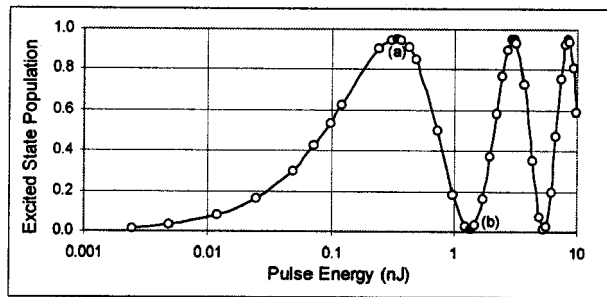


Figure 7. The excited state population of potassium is plotted as a function of pulse energy. Circles indicate that the data point is a simulation result. The connecting lines are not actual simulation data, but only included to aid in visualization.

Initially, the excited state population scales linearly with pulse energy. This is the result predicted by the rate equations. However, as the energy increases, the excited state population does not saturate at a value of 0.5 as predicted by the rate equations. Instead, at 0.34 nJ (indicated by point (a) in the figure), almost all of the population is in the excited state. If the pulse energy is increased still further, the population is stimulated back towards the ground state. At point (b), almost all of the population is back in the ground state. The excited state population and the laser attenuation for a pulse with energy (b) are both plotted as a function of time in Figure 8. Since little collisional relaxation occurs on

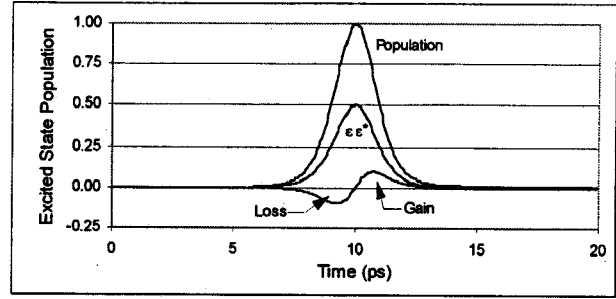


Figure 8. The time history of the excited state population and the pulse gain are shown for a 1.3 nJ pulse after propagating through 2 mm of potassium at 10^{11} cm^{-3} . This corresponds to point (b) in Figure 7.

these short time scales, conservation of energy dictates that this pulse sees very little integrated attenuation. This is shown in the figure, where the first half of the pulse is attenuated, and the second half experiences gain. The time-integrated gain is approximately zero. This behavior has been extensively studied, and is termed "self-induced transparency." McCall and Hahn¹⁸ wrote the definitive paper on this subject in 1969.

An interesting phenomena occurs as the pulse energy is increased beyond point (a) in Figure 7. The population then flops back and forth during the pulse. If the electric field of the pulse is constant, these oscillations occur at a fixed frequency, the Rabi frequency (Ω_{Rabi}). In general, the Rabi frequency is time-dependent and is related to the electric field envelope by

$$\Omega_{\text{Rabi}} = \frac{\mu_{21}\epsilon(t)}{\hbar} \quad (31)$$

Figure 9 shows the Rabi oscillation corresponding to the maximum pulse we can produce with our unamplified

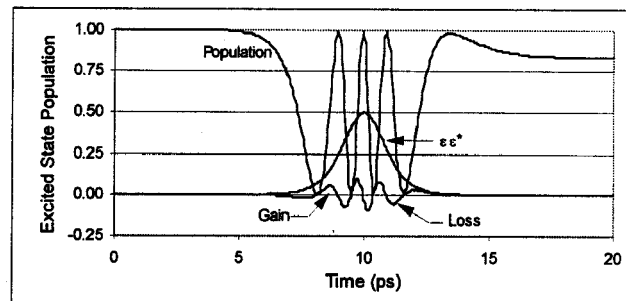


Figure 9. The time history of the excited state population and the pulse gain are shown for a 22.6 nJ pulse after propagating through 2 mm of potassium at 10^{11} cm^{-3} . This corresponds to the maximum pulse energy for our unamplified Ti:sapphire laser.

Ti:sapphire laser. The pulse energy is 22.6 nJ. Although this phenomena is interesting, for our purposes, it is undesirable to operate in this regime. The state of the atomic population following a pulse that induces Rabi oscillations is highly sensitive to pulse shape, height, and duration. Slight laser fluctuations result in very unpredictable behavior, and this makes correct characterization of the pump/probe experiment not possible.

Pump/Probe Propagation

The previous results, shown in Figure 7, suggest that potassium pump/probe will most likely be linear when pulse energies are less than 0.1 nJ. For preliminary investigation, we decided to consider a probe energy of 1.2 pJ (100 μ W average power). We varied the pump energies from 1.2 pJ to 122 pJ. We have simulation results for these pump and pulse energies with the product of the total number density and the interaction length, $N_{TOT}L$, varying from 2×10^9 to 2×10^{12} mm cm⁻³. Currently, numerical errors prevent us from obtaining results with $N_{TOT}L < 2 \times 10^9$ mm cm⁻³. This issue will be addressed in a future version of the code.

We are looking for a linear relationship between modulation depth and the $N_{TOT}L$ product, such as:

$$\alpha_{MOD} = C N_{TOT}L \quad (32).$$

To determine if such a relationship exists, we solved equation (32) for C , and plotted that result in Figure 10. As an example, when the pump pulse energy is 24 pJ, the constant in equation (32) is approximately -0.5×10^{-14} , where N_{TOT} is given in cm⁻³, and L is given in mm. This relationship holds provided that the $N_{TOT}L$ product does not exceed 3×10^{11} mm cm⁻³. Similar limits can be defined for other pump energies.

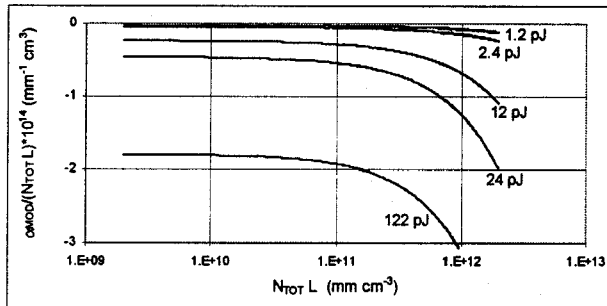


Figure 10. Linearity of pump/probe modulation depth with $N_{TOT}L$ for several values of pump pulse energy. The probe pulse energy is 1.2 pJ.

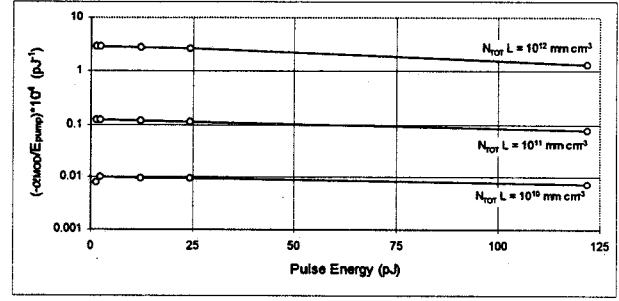


Figure 11. Linearity of pump/probe modulation depth with pulse energy for several values of $N_{TOT}L$. The probe pulse energy is 1.2 pJ. Circles indicate the data point is a simulation result. The connecting lines are not actual simulation data, but only included to aid in visualization of departure from linearity.

A similar presentation of the data can be made to check for linearity of the pump/probe signal with pump pulse energy. In this case we assume the following relationship.

$$\alpha_{MOD} = K E_{PUMP} \quad (33)$$

Figure 11 plots K as a function of the pulse energies shown in Figure 10. Clearly, for pump energies less than 25 pJ, this relationship applies fairly well. However, it does not hold between 25 pJ and 122 pJ.

We conclude, therefore, that it will be possible to perform picosecond pump/probe experiments within well-defined rate equation limits, which are in agreement with the limits originally set by Fiechtner *et al.*² Whether the density matrix formalism predicts the same modulation depth as the rate equations is another question.

Comparison Between the Rate Equation and Density Matrix Formalisms

We find that, when realistic numbers are used in both the rate equation and the density matrix formalisms, the two approaches always agree to within an order of magnitude - when we remain within the rate equation limit. Indeed, it is possible to force complete agreement by adjusting the phase shift between the pump and probe pulses in the density matrix model. This is a reflection of a point we have already made - very slight changes in Δz , on the order of a fraction of an optical wavelength, can dramatically change the pulse envelope function. For example, if Δz is set so that the envelope is purely real, coherences due to the pump pulse are exactly in phase with the probe pulse. If Δz is then shifted one-half of an optical wavelength, the pump and probe are exactly out of phase. These seemingly minor

phase shifts can significantly change the modulation depth predicted by the model. Shifts of this magnitude will most definitely occur in an experiment. At this point in time, encouraging rough agreement has been found. In order to explore this question accurately, however, it will be necessary to average the modulation depth predicted by the density matrix model over the phase shifts one should encounter in a real experiment. That work is ongoing.

Conclusions

This paper presents a basic discussion of both rate equation and a density matrix models that we are currently developing to study pulse propagation in pump/probe experiments. The non-perturbative density matrix model does not use any simplifying assumptions with regards to pulse intensities, and treats the atomic response with a quantum-mechanically-correct formalism. This model is being developed in an attempt to either validate the rate equation-based model or to identify a similar kind of relationship. Furthermore, the model can be used to maximize signal while staying within the experimental limits of applicability of this relationship.

Preliminary simulation results were presented to demonstrate qualitative behavior as a function of both pump pulse energy and total number density. Experimental parameters for a potassium pump/probe experiment were used, and the simulations demonstrated linear behavior in the weak interaction limit. However, a departure from this linearity was observed as the interaction strength was increased. When the laser pulses are sufficiently strong to cause Rabi oscillations in the atomic populations, it is no longer possible to characterize the experiment with simple expressions. In this regime, subtle changes in pulse amplitude and shape can result in dramatically different modulation depths.

In order to accurately compare the rate equation and density matrix formalisms, it will be necessary to average the modulation depth predicted by the density matrix model over the phase shifts one should encounter in a real experiment. Future work will also include the implementation of multi-level models for the atomic resonance. A fully accurate potassium model requires that the three-level density matrix equations are used, although the Potassium D lines are sufficiently separated that the two-level model contains most of the important physics. Following some basic improvements to the numerical code, we will simulate potassium pump/probe propagation, and thoroughly characterize the parameter space. This will involve careful experimentation, including real-time pump/probe and line-of-sight absorption measurements over the range of

concentrations and laser intensities of interest. Measurements will then be compared to the predictions of the density matrix and rate equation formalisms.

Acknowledgments

This research has been supported by the National Science Foundation through grants CTS-9411391, CTS-9711889, and DGE-9554559, and by the US Air Force Wright Laboratories through grant number F33615-96-C-2632.

References

1. G.J. Fiechtner and M.A. Linne, "Absolute Concentrations of Potassium by Picosecond Pump/Probe Absorption in Fluctuating, Atmospheric Flames", *Combust. Sci. and Tech.*, Vol. 100, 11-27, (1994).
2. G.J. Fiechtner, G.B. King, and N.M. Laurendeau, "Rate-equation model for quantitative concentration measurements in flames with picosecond pump-probe absorption spectroscopy", *Appl. Opt.*, Vol. 34, No. 6, 1108-1116, (1995).
3. J. P. Heritage, "Picosecond nonlinear spectroscopy of silver microstructures and surface absorbates", in B.A. Gartez and J.R. Lombardi (Ed), *Advances in Laser Spectroscopy 2*, John Wiley & Sons Ltd., New York, NY, 207-224, (1983).
4. T. Settersten and M. Linne, "Two-Level Rate Equation Based Model for Single-Point Picosecond Pump/Probe Measurements of Molecular Populations", technical note # CCER97-002, Center for Combustion and Environmental Research, Colorado School of Mines, (1997).
5. T. Settersten and M. Linne, "Two-Level Rate Equation Based Model Results for Single-Point Picosecond Pump/Probe Measurements of CH", technical note # CCER97-003, Center for Combustion and Environmental Research, Colorado School of Mines, (1997).
6. J. Luque and D.R. Crosley, "LIFBASE: Database and Spectral Simulation program (Version 1.0)", SRI Internal Report MP 96-001, (1996).
7. J. Luque and D.R. Crosley, "Electronic transition moment and rotational transition probabilities in the CH A-X system", *J. Chem. Phys.*, **104**, 2146, (1996).
8. J. Luque and D.R. Crosley, "Electronic transition moment and rotational transition probabilities in the CH B-X system", *J. Chem. Phys.*, **104**, 3907, (1996).
9. M. Zachwieja, "New investigations of the A-X band system in the CH radical and a new reduction

- of the vibration-rotation spectrum from ATMOS spectra", J. Mol. Spectros., **170**, 285, (1995).
10. J.J. Sakurai, *Modern Quantum Mechanics*, Addison-Wesley Publishing Company, Inc., New York, NY, (1985).
 11. J.R. Lalanne, A. Ducasse, and S. Kielich, *Laser-Molecule Interaction: Laser Physics and Molecular Nonlinear Optics* (John Wiley & Sons, Inc., New York, NY, 1996).
 12. R.W. Boyd, *Nonlinear Optics*, Academic Press, San Diego, CA, (1992).
 13. J.T. Verdeyen, *Laser Electronics*, Third Edition, Prentice Hall, Englewood Cliffs, NJ, (1995).
 14. Ref. 7, p. 195.
 15. W.H. Press, S.A. Teukolsky, W.T. Vetterling, and B.P. Flannery, *Numerical Recipes in C: the Art of Scientific Computing, Second Edition* (Cambridge University Press, New York, NY, 1992), pp. 707.
 16. G.J. Fiechtner, Quantitative Concentration Measurements in Atmospheric-Pressure Flames by Picosecond Pump/Probe Absorption Spectroscopy, Ph.D. dissertation, Purdue University (1992).
 17. W.L. Wiese, M.W. Smith, and B.M. Glennon, *Atomic Transition Probabilities (Na through Ca - A Critical Data Compilation)*, National Standard Reference Series, National Bureau of Standards 22, Volume II, U.S. Government Printing Office, Washington D.C. (1966).
 18. S.L. McCall and E.L. Hahn, "Self-Induced Transparency," Phys. Rev. **183**(2), 457, (1969)